Digest Journal of
Nanomaterials and Biostructures

Dig. J. Nanomater. Bios. **2026**; 21(2): 55196
https://doi.org/10.31083/DJNB55196

Original Research

Al_2O_3 Nanoparticles Synthesized Using Plant Extracts: Characterization and Application to Glucose Sensing

Lamia K. Abbas[1], Najwa J. Jubier[2], Hanan Abd Ali Thjeel Al-Ogaili[2,]*

[1]Department of Physics, College of Science, University of Baghdad, 10070 Baghdad, Iraq
[2]Department of Physics, College of Science, Wasit University, 52001 Kut, Iraq
*Correspondence: hananabd81@gmail.com (Hanan Abd Ali Thjeel Al-Ogaili)

Academic Editor: Carmen-Georgeta Ristoscu
Submitted: 28 December 2025 Revised: 14 April 2026 Accepted: 30 April 2026 Published: 23 June 2026

Abstract

α-Al_2O_3 nanoparticles (NPs) were sustainably and cost-effectively synthesized using *Cinnamomum verum* and laurel (*Laurus nobilis*) leaf extracts (samples J1 and J2, respectively) and characterized in terms of their structural, morphological, optical, and electrochemical properties. Both samples featured the desired hexagonal crystal structure, and the average crystallite sizes of pure Al_2O_3 , J1, and J2 were determined as approximately 16.90, 32.42, and 32.44 nm, respectively. The X-ray diffraction patterns of J1 and J2 matched the standard diffraction pattern of pure Al_2O_3. Scanning electron microscopy measurements revealed that J1 and J2 contained well-dispersed uniform-morphology particles with average sizes of 26.33 and 27.9 nm, respectively. Diffuse reflectance spectroscopy measurements revealed that J1 and J2 comprised spherical particles and featured optical band gaps of 4.4 and 4.5 eV, respectively. The Fourier transform infrared spectra of J1 and J2 featured Al–O bond peaks in the range of 500–650 cm^{-1}, and cyclic voltammetry measurements performed for an α-Al_2O_3 NP electrode revealed its responsiveness to glucose, which was ascribed to a surface-controlled adsorption process. The peak broadening, changes in potential, and charge transfer enhancement observed with increasing glucose concentration suggested that electrochemical behavior was controlled by interfacial contact rather than diffusion. The estimated limit of detection (6 mM) revealed moderate sensitivity to glucose, suggesting the potential utility of α-Al_2O_3 NPs as an electrode material for electrochemical glucose sensing.

Keywords: Al_2O_3; nanoparticle; plant extract; green route; laurel leaves; *Cinnamomum verum*

1. Introduction

Aluminium oxide (Al_2O_3), also known as alumina is one of the most important engineering ceramic materials developed during the second half of the twentieth century due to its excellent chemical and physical properties, including high chemical stability, exceptional hardness, and a high melting point of approximately 2045 °C [1]. These properties make Al_2O_3 widely used in various technological and industrial applications. Aluminium oxide exists in several crystalline phases, among which α-Al_2O_3 and γ-Al_2O_3 are the most stable and widely studied forms. Both phases consist of aluminium and oxygen atoms in the same stoichiometric ratio, but they differ in their crystal structures. The α-Al_2O_3 phase has a hexagonal crystal structure, representing the thermodynamically stable phase, whereas γ-Al_2O_3 typically exhibits a tetragonal or defect spinel structure and is often considered a porous or partially amorphous material [1,2]. Due to their nanoscale size, Al_2O_3 nanoparticles exhibit unique properties, such as enhanced chemical reactivity, optical behaviour, electrical characteristics, catalytic activity, and thermal stability, these features make Al_2O_3 nanoparticles (NPs) suitable for applications in ceramics, catalysis, nanocomposites, paints, refractory materials, biomedical systems, capacitor and sensors, In particular [3,4], their high surface-to-volume ratio makes them promising for electrochemical sensing applications. Glucose is a vital monosaccharide whose abnormal concentration in blood is closely associated with diabetes and its serious complications, including cardiovascular, kidney, and vision disorders. Therefore, reliable and stable methods for glucose detection are essential for effective disease monitoring. Both enzymatic and non-enzymatic electrochemical sensors are used for glucose detection; however, non-enzymatic sensors offer advantages such as higher stability, sensitivity, and resistance to environmental conditions. Various nanomaterials, including noble metals, metal–organic frameworks, and two-dimensional materials, have been widely employed in enzyme-free glucose sensors due to their high surface area and enhanced electrochemical activity [5,6]. In particular, gold nanoparticles (Au NPs) have shown excellent biocompatibility and sensitivity, achieving very low detection limits. However, conventional synthesis methods of such nanomaterials often leave organic residues or by-products on the surface, which can interfere with electrochemical performance [7]. This highlights the need for clean, stable, and environmentally friendly nanomaterials for glucose sensing applications.

Various methods have been developed for synthesizing aluminium oxide nanoparticles, including co-precipitation, wet impregnation, sol–gel techniques, and biosynthesis using biological resources [8,9,10,11]. Recently, green routes using plant extracts have gained considerable attention because they provide an eco-friendly, cost-effective, and sustainable alternative to conventional chemical synthesis. Plant extracts contain natural biomolecules such as phenols, flavonoids, and proteins, which act as reducing and stabilizing agents during nanoparticle formation, leading to nanoparticles with improved size control, stability, and morphology. Among natural resources, laurel leaves (*Laurus nobilis*) and *Cinnamomum verum* have attracted interest due to their rich content of bioactive compounds with strong antioxidant properties, making them suitable candidates for the green synthesis of Al_2O_3 nanoparticles for electrochemical sensing applications.

The *Cinnamomum verum* is tropical plants that is widely cultivated in Southeast Asia. Its bark and leaves are rich in essential oils that are used as spices and in traditional medicine to treat colds, stomach problems, high blood sugar, and pain. Phytochemical studies have identified many bioactive compounds, such as, diterpenes, monoterpenes, sesquiterpenoids, Cinnamaldehyde, cinnamyl acetate, cinnamic acid, eugenol, linalool, phenolic compounds, flavonoids, and tannins, these compounds contain reactive functional groups that facilitate interaction with metal ions. These functional groups make it easier for Al^{3+} ions to combine with solution, which helps control the formation of aluminum hydroxide intermediates and keeps particles from sticking together by naturally capping them. This phytochemical makeup explains why these plant extracts work so well at controlling the green synthesis of α-Al_2O_3 NPs [12,13]. Similarly, *Laurus nobilis*, is rich with the main chemical compounds like, terpenoids, flavonoids, fatty acids, alkaloids, phenolic, and organic acids which contains hydroxyl (–OH) and carboxyl (–COOH) functional groups, these reactive molecules that can interact with metal ions [14,15] i.e. these compounds enable the reduction of metal ions and encourage the production of stable nanoparticles [16,17].

The synthesis of various phases of Al_2O_3 using natural plant materials has been demonstrated in several studies such as, date palm seed extract [18], Mentha Pulegium [19] and Aloe Vera [20]. Most of the studies focused on characteristics and applications of γ-$Al_2O_{3,}$ such as Nemade et al. [21], which examined the photovoltaic and supercapacitive. While other authors have shown that nanosized γ-Al_2O_3 nanoparticles prepared by physical/chemical methods possess a nanoscale structure, semiconducting behaviour, and improved charge transfer properties, which are promising for electrochemical sensors and photo-catalysts [22], Additionally, γ-Al_2O_3 synthesized via probe sonication demonstrated good electrochemical performance and high sensitivity for paracetamol detection, confirming its suitability for electrochemical sensing [23]. Kuoloud et al. [24] also highlighted the biomedical potential of γ-Al_2O_3 nanoparticles due to their anti-inflammatory and immunomodulatory properties .

In other studies, α-Al_2O_3 NPs have been synthesized using plant extracts like date palm seed extract, where phytochemicals have been found to act as reducing and stabilizing agents, producing nanoscale particles with a high degree of purity and biological activity. By demonstrating their eco-friendly nature, plant-mediated synthesis not only enhances nanoparticle application in biomedical, environmental, and antimicrobial fields, but it also offers an eco-friendly route for nanoparticle production [18,25,26].

Despite the increasing interest in plant-mediated nanomaterial synthesis for metal oxide nanoparticles, most literature focuses on γ-Al_2O_3, while limited attention has been given to the plant-driven synthesis of highly crystalline α-Al_2O_3 NPs and their electrochemical applications.

Furthermore, the relationship among green synthesis, optical band gap properties, and electrochemical performance of α-Al_2O_3 NPs remains inadequately investigated. Therefore, the recent study aims to fill the research gap by examining the green synthesis of α-Al_2O_3 NPs for wo plant extracts (*Cinnamomum verum* and Laurel leaves), and correlating their structural, optical, and electrochemical characteristics. In the present study, α-Al_2O_3 NPs were synthesized using extracts from these two plants, and their structural, optical, and morphological properties were systematically characterized. In addition, their electrochemical behavior was investigated using cyclic voltammetry (CV), that can be applied as electrochemical bio-sensing electrodes for detecting biologically important molecules like, glucose.

2. Materials and Methods

2.1 Material

Aluminium nitrate nonahydrate ($Al(NO_3)_3 \cdot 9H_2O$) 99.99, weight 4 g of *Cinnamomum verum* laurel leaf with [1M] for both plants. The samples of both laurel leaf and the *Cinnamomum verum* have been supplied from local markets in Wasit (Iraq), distilled water, and sodium hydroxide (purity 98.99).

2.2 Syntheses of AL_2O_3 NPS from the Plant Extract

Using fresh samples of cinnamon verum (J1) and *Laurus nobilis* (J2) purchased from a local market, in order to remove contaminants from two plants must be rinsed and dried at 37 °C. Mixing (4 g) of cinnamon verum (J1) with 50 mL deionized water will result in a reddish-purple product for cinnamon verum (J1) whereas product is green color for *Laurus nobilis* (J2). Then heat it at 60 °C for 30 minutes with continuous stirring. After cooling to room temperature, the samples will be filtered using (Whatman type filter paper), and separated using a centrifuge (3000 rpm/minute) for (20 minutes) to produce aqueous extracts for two plants that contain extract bioactive phytochemicals, an aqueous precursor solution was prepared by dissolving 18.756 g of aluminium nitrate nonahydrate ($Al(NO_3)_3 \cdot 9H_2O$) in 50 mL of deionized water to obtain a 1 M solution. The solution

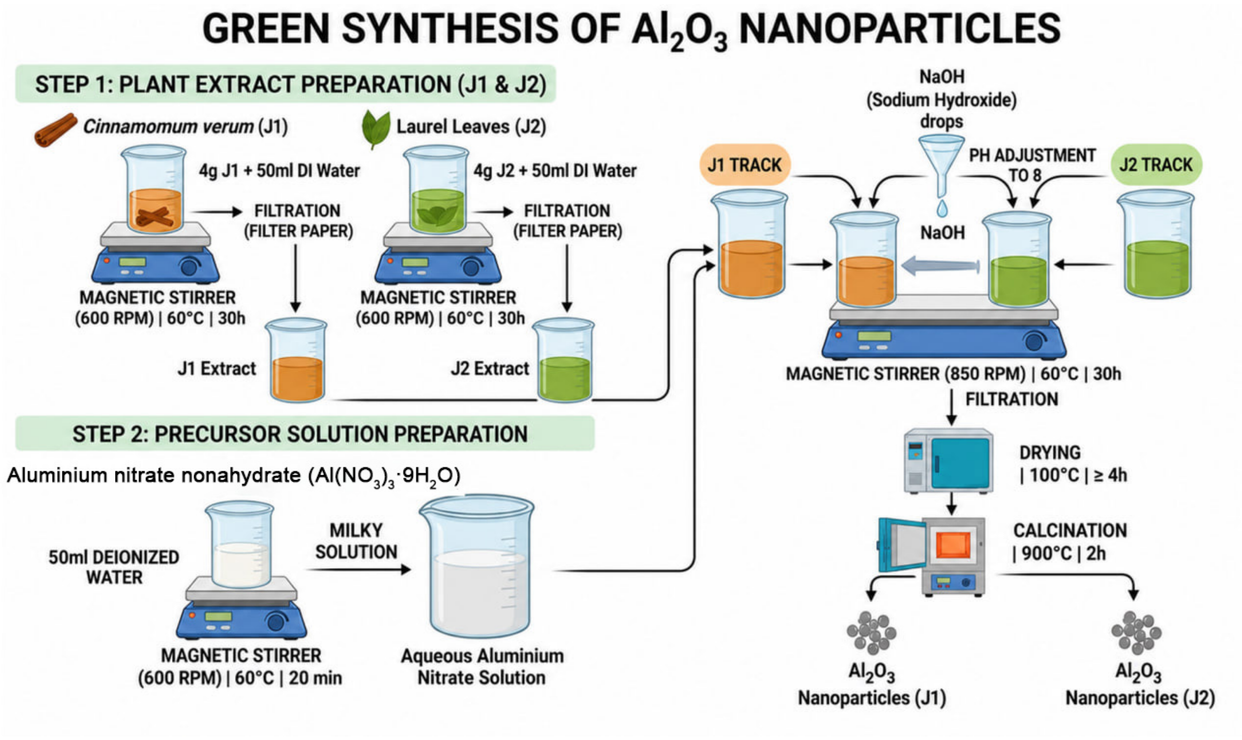

Fig. 1. Diagram illustrating all preparation steps of both samples J1 and J2 of α-Al_2O_3 NPs.

was stirred at 600 rpm at 60 °C for 20 min until a homogeneous solution was formed, as a next step, 50 mL of plant extract were added dropwise to the precursor solution for 30 hours under continuous stirring at 850 rpm and 60 °C. In order for aluminum hydroxide precursors to precipitate effectively, the pH was carefully adjusted by adding drops of 0.1 M NaOH solution during the reaction. When the reaction was completed, the suspension was filtered and dried at 100 °C for four hours. A muffle furnace was used to calcine the dried powder for two hours at 900 °C to produce crystalline Al_2O_3 nanoparticles. The synthesis process was repeated three times to ensure reproducibility. After that, these nanoparticles were used in electrochemical applications, particularly for cyclic voltammetry (CV) analysis. A schematic diagram illustrating the preparation procedure is presented in Fig. 1.

2.3 The Formation of Nanoparticles

The active role of phytochemicals found in these plants, such as phenolic substances, flavonoids, terpenoids, and organic acids, explains how *Cinnamomum verum* and *Laurus nobilis* extracts were used to make α-Al_2O_3 NPs in a green route. These bioactive chemicals have functional groups (–OH, –COOH) that can react with aluminum ions (Al^{3+}) in the starting solution.

At first, these substances connect with Al^{3+} ions, which causes controlled nucleation and the creation of aluminum hydroxide ($Al(OH)_3$) intermediates when the pH is raised to about 8. At this point, the organic molecules keep the particles from growing out of control and sticking together, stopping them from fixing and capping. The organic parts break down when the mixture is dried and then heated to 900 °C. The aluminum hydroxide precursor changes into solid α-Al_2O_3 NPs. Nanoparticles with a fixed size and shape are the end result of the phytochemical stabilization process. This process shows how important phytochemicals from plants are for controlling the formation, stability, and size of nanoparticles in the green synthesis route.

2.4 Electrochemical Measurements

Materials Required of Electrochemical System: Electrochemical workstation (potentiostat/galvanostat), Three-electrode system: Working electrode (WE): α-Al_2O_3 NPs, reference electrode (RE): Ag/AgCl, Counter electrode (CE): Carbon.

Procedure:

Preparation of the Electrochemical Cell: Prepare the electrolyte and sample solution.

Prepare a sample solution, if testing a specific analyte, prepare a standard concentration (for this test 1 mM glucose 5 mM and was prepared).

- Setup of the Electrochemical System

1. Connect the screen-printed electrode to the potentiostat.
2. Ensure proper electrical contact between the electrodes and the potentiostat.
3. Running the Electrochemical Test.
4. To test the control or blank, place 50 µL from the sample on screen printed electrode.
5. Choose the appropriate technique.

6. Cyclic Voltammetry (CV) for redox properties.

7. Input test parameters (e.g., voltage range, scan rate, frequency).

8. Start the experiment and record data.

9.10 µL of analyte is added to the sample on the screen-printed electrode. The same tests are repeated.

3. Results

3.1 X-ray Diffraction (XRD)

The crystalline structure of the produced α-Al_2O_3 NPs, created under identical conditions, was optimized and duplicated several times using two plant extracts, as analyzed by X-ray diffraction (XRD) analysis was carried out using an XRD-7000/XRD-7000S diffractometer (Shimadzu Corporation, Kyoto, Japan), seen in Fig. 2. The diffraction angles and intensities of the observed peaks are consistent with previously reported XRD patterns of α-Al_2O_3 NPs [19,27]. The XRD pattern indicates that the samples consist of a single crystalline phase of α-Al_2O_3 NPs with a hexagonal structure. where the average crystal size of α-Al_2O_3 NPs was calculated by Scherer's Eqn. 1.

$$D = \frac{0.9\lambda}{BCos\theta} \quad (1)$$

The calculated average crystallite sizes were approximately 16.90 nm for α-Al_2O_3 NPs (pure), 32.42 nm for sample J1, and 32.44 nm for sample J2, as mentioned in Table 1. The absence of additional diffraction peaks indicates that no impurities or precursor compounds are present, confirming the high purity and successful crystallisation of the synthesized nanoparticles.

The XRD pattern of pure α-Al_2O_3 shows strong diffraction peaks corresponding to the planes (111), (212), (222), (311), (400), and (404) at 2θ values of 37.63°, 46.46°, and 67.58°, which agree with JCPDS card No. 96-200-2890. For the plant-mediated samples, J1 exhibited peaks at (012), (200), and (302) with 2θ values of 30.2°, 33.56°, and 58.04°, while for J2 the planes appeared at (012), (200), and (302) at 30.39°, 33.75°, and 58.23°, respectively. These results for J1 and J2 are showing excellent agreement with JCPCS card No. 96-200-2893X, confirming the formation of crystalline α-Al_2O_3 NPs for two samples.

The growth of α-alumina crystallites is strongly influenced by thermal treatment. At elevated temperatures, nanoparticles become more mobile and interact with each other, leading to particle coarsening and crystallite growth. This process results in an increase in inter-particle distances and a reduction in the number of smaller particles, ultimately producing larger crystallites.

As the temperature increases, the coarsening rate also increases, accelerating crystallite growth. This phenomenon depends on several factors, including temperature, initial crystallite size, and ion concentration in the solution [28]. Previous studies have shown that the formation of crystalline α-Al_2O_3 occurs through a series of polymorphic phase transformations, where intermediate phases gradually transform into the thermodynamically stable α-phase, known for its high thermal stability and excellent structural properties, The XRD results confirmed the successful formation of crystalline α-Al_2O_3 nanoparticles, with average crystallite sizes of approximately 16 nm for pure α-Al_2O_3 NPs and 32.42 nm and 32.44 nm for samples J1 and J2, respectively. Furthermore, FE-SEM analysis revealed nanoscale particles with average sizes of approximately 26.33 nm for J1 and 27.9 nm for J2, indicating relatively uniform morphology and good dispersion.

3.2 Transmission Electron Microscopy(TEM)and FE-SEM Results

The TEM images(HT7700, Hitachi High-Tech Corporation, Tokyo, Japan) coupled with the associated histogram Fig. 3 show that α-Al_2O_3 NPs were successfully formed at the optimum temperature using the two plant extract solutions, J1 and J2. The TEM observations clearly revealed the formation of well-defined nanoparticle-like structures. These results confirm the successful synthesis of α-Al_2O_3 powder with relatively uniform and predominantly spherical morphology.

The average particle size of the α-Al_2O_3 NPs was calculated from the TEM images, ranging between 12 and 50 nm for J1 and J2, which is in reasonable agreement with the crystallite size estimated from XRD analysis. Furthermore, these results provide valuable insights into the surface morphology and particle size distribution of the synthesized α-Al_2O_3 nanoparticles.

Such information is important for understanding the formation mechanism of α-Al_2O_3 and can contribute to improving their synthesis process and enhancing their efficiency in various applications [29,30]. In addition, TEM results suggest that the phytochemical components present in the plant extracts form a capping layer around the α-Al_2O_3 NPs, indicating that the plant extracts act as natural stabilizing and capping agents, which control nanoparticle growth during the synthesis process.

FE-SEM analysis (Carl Zeiss Microscopy GmbH, Oberkochen, Germany)showed that the synthesised α-Al_2O_3 NPs possessed a relatively uniform size and spherical morphology, with some particles forming small clusters. The use of plant extracts proved to be an effective and eco-friendly approach for the green synthesis of Al_2 O_3 nanoparticles.

As shown in Fig. 4, the average particle sizes were approximately 26.33 nm and 27.9 nm for samples J1 and J2 of α-Al_2 O_3 NPs, respectively, as shown in Fig. 4 histogram analysis of the particle size distribution of α-Al_2O_3 NPs synthesized using J1 and J2. The results indicate that the α-Al_2O_3 NPs have particle sizes ranging between 20–50 nm, with a predominantly spherical shape and homogeneous composition.

Table 1. Parameters XRD of Al_2O_3 NPs for (pure, J1 and J2).

Sample	α-Al_2O_3			α-Al_2O_3 (J1)			α-Al_2O_3 (J2)		
2 θ° (Deg.)	**Strongest 3 Peaks**			**Strongest 3 Peaks**			**Strongest 3 Peaks**		
	37.63	46.46	67.58	30.20	33.56	58.04	30.39	33.75	58.23
hkl	311	400	404	012	200	302	012	200	302
d_{hkl} Exp.(A°)	2.388	1.952	1.385	2.957	2.668	1.588	2.939	2.654	1.583
d_{hkl} Std.(A°)	2.378	1.971	1.394	2.942	2.649	1.580	2.942	2.649	1.580
The crystallite size (nm)	13.263	21.639	17.276	34.28	34.57	28.39	34.30	34.59	28.42
Average crystallite size (nm)	16.90			32.42			32.44		
Card No.	96-153-1490			96-200-2893			96-200-2893		

XRD, X-ray diffraction; NPs, nanoparticles.

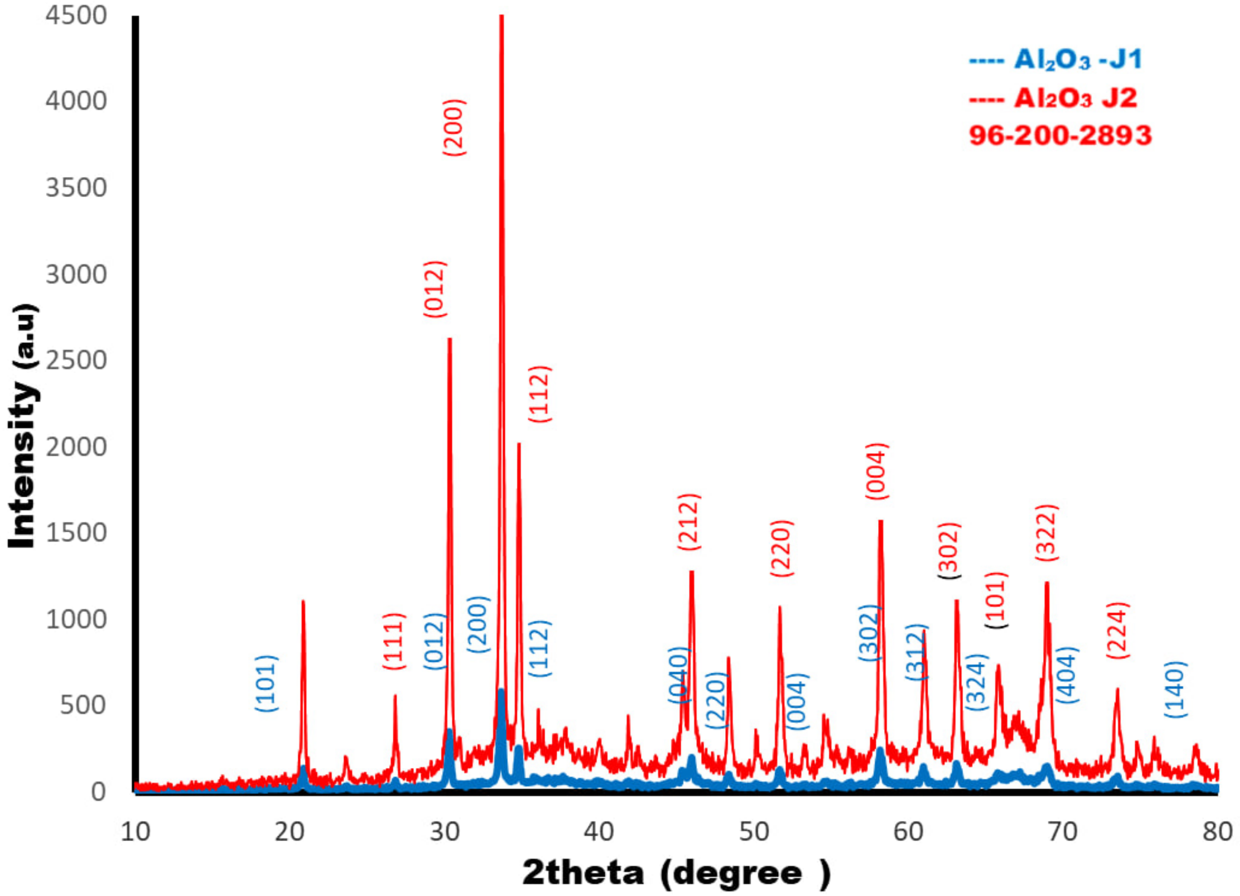

Fig. 2. XRD of Al_2O_3 NPs of J1 and J2.

Furthermore, the FE-SEM images Fig. 4 revealed that the synthesized Al_2O_3 NPs were homogeneous, uniformly distributed, and free from visible cracks or structural defects. These observations confirm the successful formation of well-defined α-Al_2O_3 nanoparticles through the green synthesis.

3.3 Diffuse Reflectance Spectroscopy (DRS)

The optical properties of α-Al_2O_3 NPs synthesized using plant extracts J1 and J2 were investigated and found to have a high light transparency and a broad spectral range. These nanoparticles exhibited excellent stability against ultraviolet radiation, thermal stability, and mechanical properties. To compute the optical band gaps of α-Al_2O_3 NPs samples made from two different plant extracts, a two-step study was carried out. The optical band gaps were estimated from the UV absorption spectra recorded in the ultraviolet region. As illustrated in Fig. 5, strong absorption peaks were observed at 280 nm for sample J1 and 275 nm for sample J2. These wavelengths correspond to photon energies of approximately 4.4 eV for J1 and 4.5 eV for J2. The band gap energies were further evaluated using the Kubelka–Munk model, which is widely employed in diffuse reflectance spectroscopy (DRS) analysis(Shimadzu

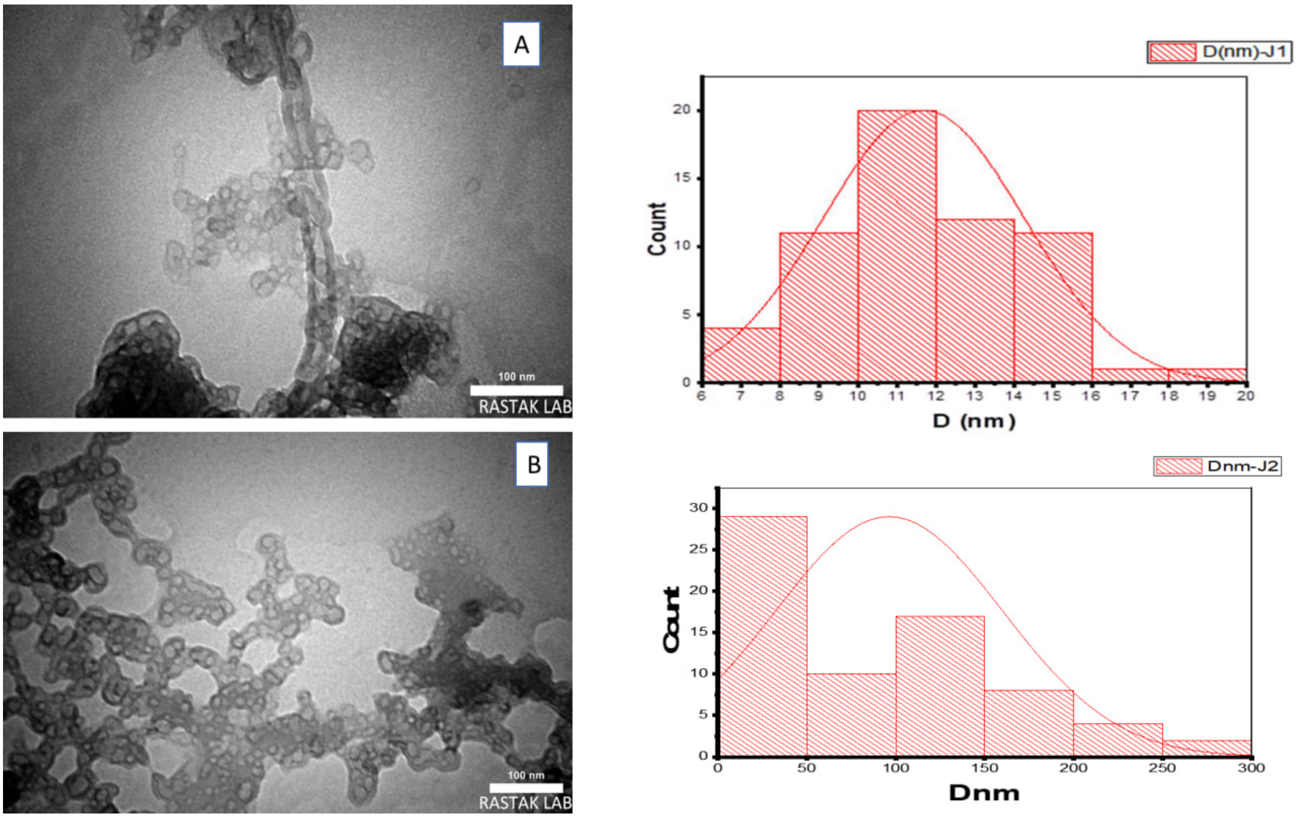

Fig. 3. TEM depict the morphology of the surface magnifying: 100 nm for Al_2O_3 NPs of (A) J1 , and (B) J2, and a histogram analysis. TEM, transmission electron microscopy. Scale bar =100 nm.

Corporation, Kyoto, Japan). The Kubelka–Munk function is expressed as follows, Eqn. 2 [31]:

$$F(R) = \frac{(1-R)^2}{2R} = \frac{K}{S} \tag{2}$$

Where:

R = reflectance at each wavelength, F(R)= K–M function (proportional to absorbance), K = absorption coefficient, S = scattering coefficient.

The optical band gap (Eg) has been determined by plotting $(F(R)\ hv)^2$ versus photon energy, a straight line was drawing along the linear portion of the curve and extending this line to intersect energy axis on an x-axis, where $(F(R)\ hv)^2 = 0$. The value of the point of intersection on the energy axis is equal to the optical ga*p* value Eg (eV).

The calculated optical band gap values were approximately 4.4 eV for sample J1 and 4.5 eV for sample J2. These relatively high band gap values may be attributed to the nanoscale nature of the synthesized α-Al_2O_3 particles and the influence of the phytochemical compounds present in the plant extracts during the synthesis process. Compared with previously reported results in the literature, the obtained band gap values are slightly lower, which could be related to differences in synthesis method, particle size, and structural properties of the samples [32]. A Tauc plot of α-Al_2O_3 NPs (sample J1 and J2) in (Fig. 5C,D) shows a direct allowed electronic transition. The linear region near the absorption edge was extrapolated to the energy axis (hv), giving a band gap of approximately 3.8–4.8 eV for J1, and 3.8, 4.6 for J2,respectively, this value is much lower than the bulk band gap (~8.8 eV) due to nanoscale effects, lattice defects, oxygen vacancies, and residual species from the green synthesis method. This material has a low band gap, which improves electron excitation and charge transfer, resulting in excellent electrochemical performance.

3.4 Fourier Transform Infrared (FTIR) Spectroscopy

The FTIR spectra (PerkinElmer 100 Optica, Waltham, MA, USA) of the synthesized α-Al_2O_3 NPs, Fig. 6 show a broad band at 3451 cm^{-1} for J1 and 3439 cm^{-1} for J2, corresponding to the O–H stretching vibration due to the adsorption of water molecules on the nanoparticle surfaces. A sharp peak at 502 cm^{-1} represents the stretching vibration of the Al–O bond, confirming the formation of pure α-Al_2O_3 NPs. The absence of other peaks indicates that organic impurities were effectively removed during high-temperature calcination.

Additional peaks at 1461 cm^{-1} (J1) and 1385 cm^{-1} (J2) are attributed to neutral oxygen species adsorbed on the surface, while peaks at 636 cm^{-1} (J1) and 635 cm^{-1} (J2) correspond to Al–O vibrations, consistent with previous reports [33]. The peak around 1050 cm^{-1} is assigned to Al–O–

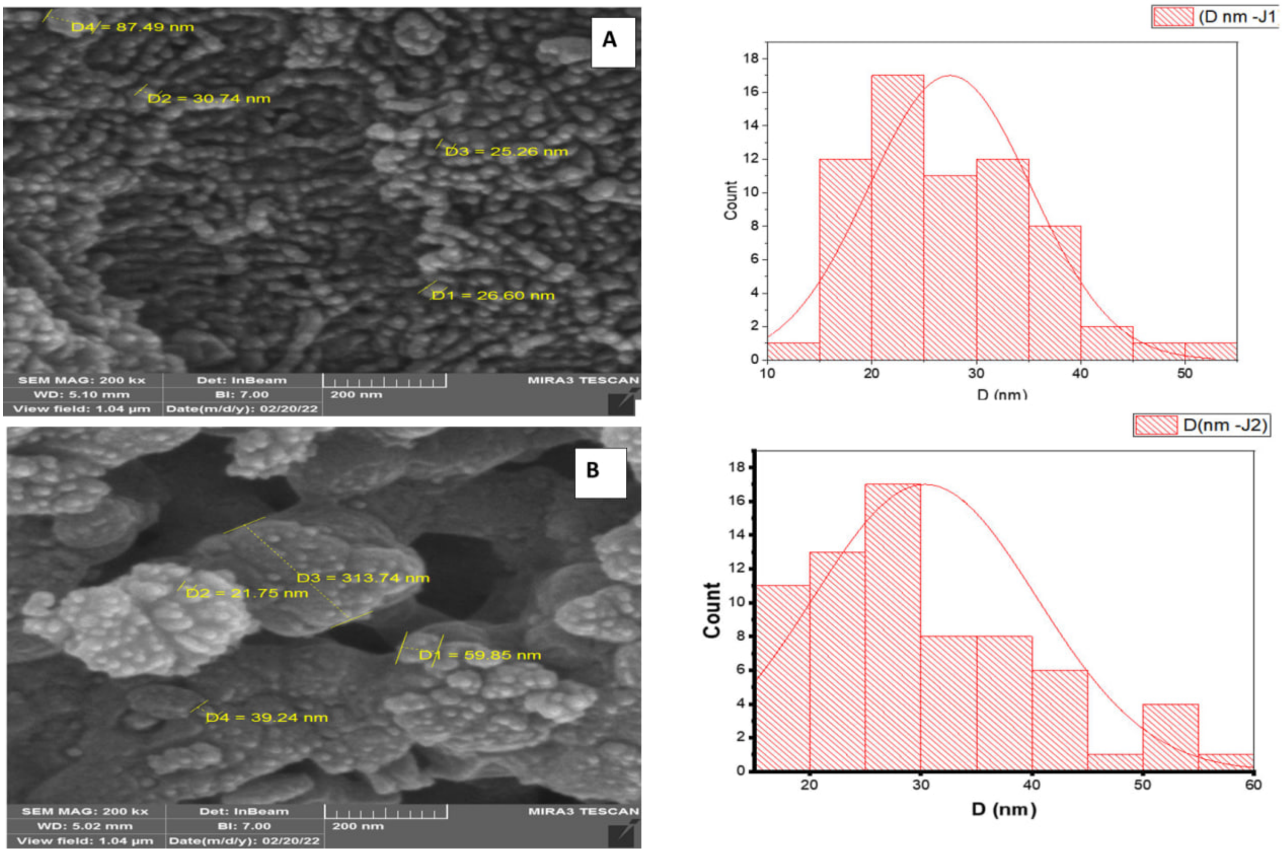

Fig. 4. FE-SEM and histogram analysis of two extract plants (A) J1 and (B) J2, of Al_2O_3 NPs. FE-SEM, field emission scanning electron microscopes; scale bar = 200 nm.

H vibrations, indicating the presence of surface hydroxyl groups, which can be seen in Table 2, which depicts the major functional groups detected in the plant extracts through FTIR analysis. The absorption bands observed existence of multiple phytochemical compounds, notably phenols, alcohols, and aromatic functional groups. These functional groups play an important role in the green synthesis by acting as reducing and stabilizing agents during the formation of α-Al_2O_3 NPs. FTIR spectroscopy is a powerful tool for material identification and provides insights into the functional groups of capping molecules in green-synthesized nanoparticles. These spectra reveal the biomolecules responsible for the reduction of metal ions and stabilization of the nanoparticles, and they offer important information about size, morphology, composition, and stability.

The FTIR results confirm that the α-Al_2O_3 NPs are highly pure, structurally stable, and of high quality.

FTIR spectra of α-Al_2 O_3 NPs indicate that the formation of a well-defined crystallized phase. For the J1 sample, the peaks were observed at 457 cm^{-1}, 502 cm^{-1}, and 635 cm^{-1}, while the J2 sample showed peaks at 458 cm^{-1}, 503 cm^{-1}, and 636 cm^{-1}. These bands correspond to the stretching modes of Al–O bonds in the octahedral structure.

Additional peaks at 818 cm^{-1} (J1) and 820 cm^{-1} (J2) are assigned to Al–O stretching in tetrahedral sites, whereas peaks at 1000 cm^{-1} (J1) and 1010 cm^{-1} (J2) correspond to Al–O–H symmetric bending vibrations, indicating the presence of surface hydroxyl groups. The peaks at 818–820 cm^{-1} also reflect the distribution of Al and H cations within the oxide lattice, consistent with previously reported studies [34,35].

According to FTIR analysis, Al–O bonding and residual functional groups exist, supporting structural information from XRD, and the presence of Al–O–H vibrations further suggests surface hydroxylation, which may contribute to the stability and functional properties of the nanoparticles as in Table 3.

3.5 Cyclic Voltammetric Analysis

Cyclic voltammetry (CV) measurements were carried out on a working electrode coated with an aluminium oxide (α-Al_2O_3 NPs) layer, a potential window from −0.50 to 0.50 V using a scan rate of 50 mV s^{-1} as in Fig. 7. The voltammograms that were collected showed a shape that stayed almost the same across several cycles with currents in the milliampere range. This means that the response is mostly due to capacitive charging, with only a little amount of faradaic redox reactions at the electrode/electrolyte interface. Peak analysis showed three separate features at −0.37, −0.06, and 0.35 V. The peak at −0.06 V had the most trans-

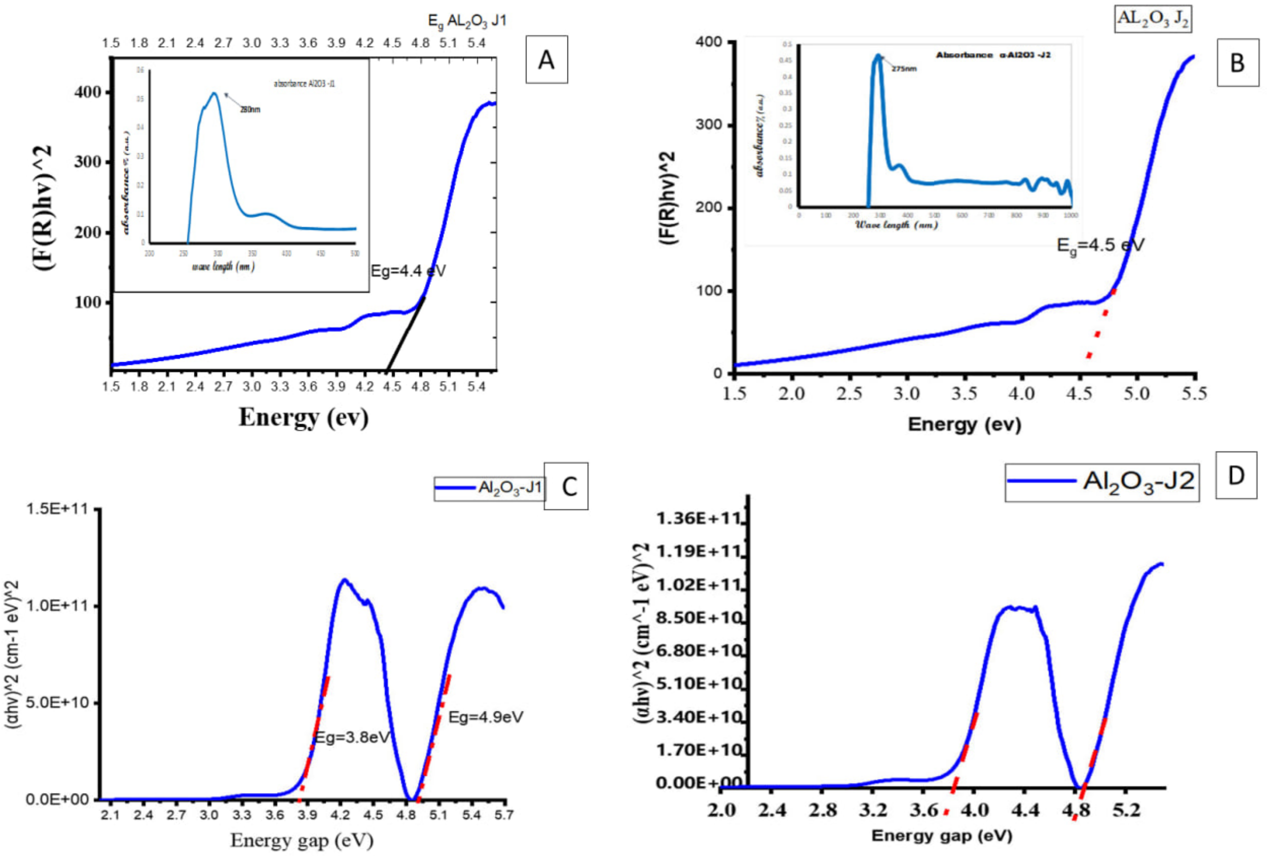

Fig. 5. DRS of α-Al_2O_3, &spectra absorbance of (A) DRS of plant J1, and (B) DRS of plant J2, (C) tauc plot of the optical bandgap for plant J1, and (D) tauc plot of the optical bandgap of plant J2. DRS, diffuse reflectance spectroscopy.

Table 2. FTIR peak assignments of plant extracts used in green synthesis of α-Al_2O_3 NPs.

Wavenumber (cm^{-1})	Functional group	*Cinnamomum verum* (J1)	Laurel leaves (J2)	Assignment
3200–3500	O–H stretching	Present	Present	Phenolic compounds and alcohol groups
3020–3080	Aromatic C–H stretching	Present	Weak/Present	Aromatic ring vibrations
2920–2850	C–H stretching	Present	Present	Aliphatic C–H groups
1680–1700	C=O stretching	Strong	Present	Aldehyde or carbonyl groups (cinnamaldehyde in J1)
1600–1630	C=C stretching	Present	Present	Aromatic ring vibration
1500–1550	Aromatic ring vibration	Present	Present	Benzene ring skeletal vibration
1200–1300	C–O stretching	Present	Present	Phenolic and alcohol groups
1000–1100	C–O–C stretching	Weak	Strong	Ether groups (e.g., cineole in J2)
700–800	Aromatic C–H bending	Present	Present	Out-of-plane bending of aromatic rings

FTIR, Fourier transform infrared spectroscopy.

Table 3. FTIR peak assignments of α-Al_2O_3 NPs (alpha phase) in green synthesis.

Wavenumber (cm^{-1})	α-Al_2O_3 (alpha phase)	Assignment
400–450	Present	Al–O bending vibration
500–600	Strong	Al–O stretching
630–650	Characteristic	Al–O vibration in α-Al_2O_3 lattice
700–800	Present	Al–O–Al bridging vibration
850–900	Usually absent	Surface Al–O groups (γ phase)
1000–1100	Weak/absent	Al–O vibrations in tetrahedral sites

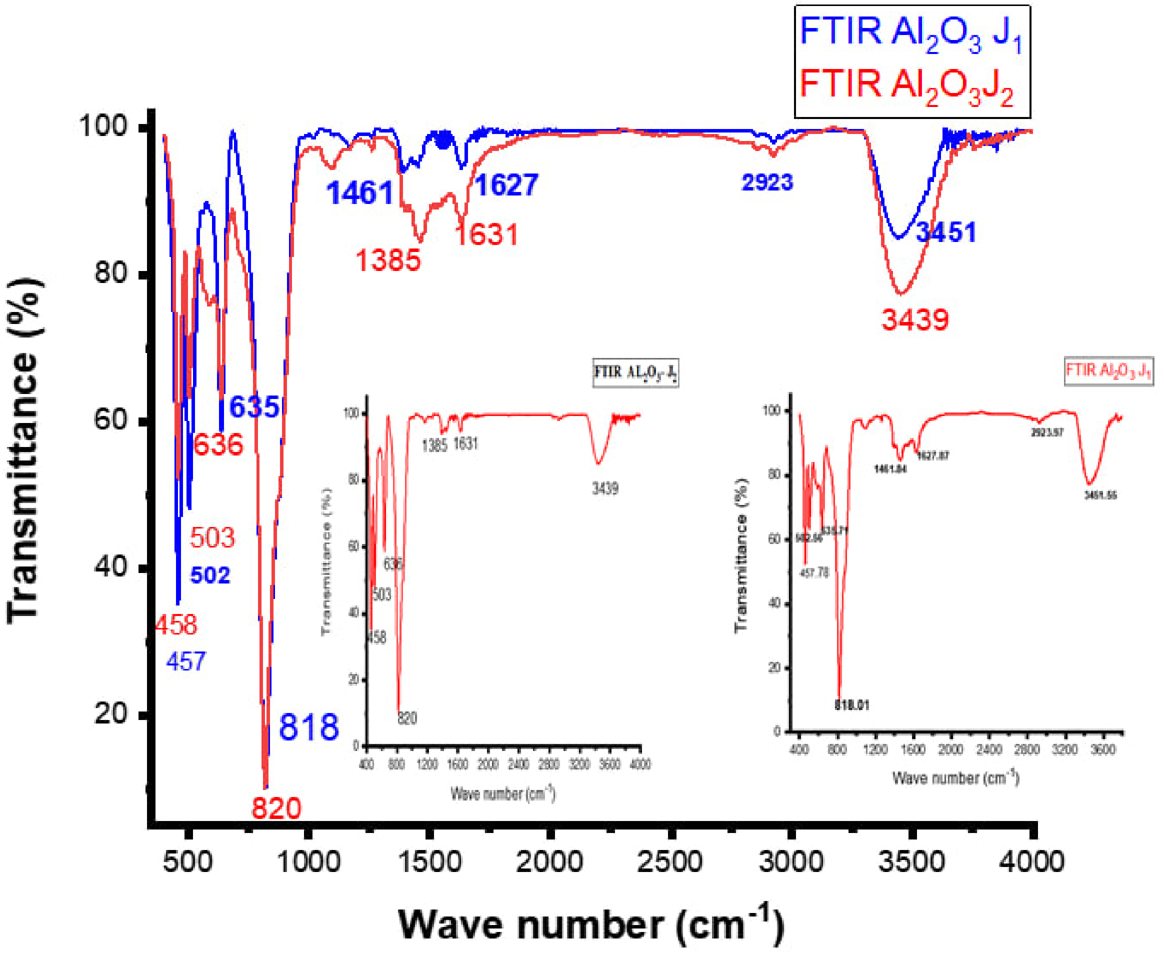

Fig. 6. FTIR of two plant extracts, J1 and J2 of α-AL_2O_3 NPs.

ferred charge (around 8 × 10^{-6} C). There were also fewer peaks in the remaining peak regions, corresponding to secondary processes.

A layer of α-Al_2O_3 NPs coating was found to restrict charge transfer and enhance interfacial stability by acting as an electrochemical barrier, as previously reported [36]. In cyclic voltammetry (CV) measurements, an increase in glucose concentration from 1 to 5 mM induces an obvious modulation in the electrochemical behaviour of the α-Al_2O_3 NPs electrode, as demonstrated by systematic shifts in peak potential, significant peak broadening, and substantial variations in the integrated charge, reflecting altered charge transfer dynamics at the electrode interface.

At 1 mM glucose, the anodic oxidation peak was centered at E_{pa} = −0.050 V, with a peak current of approximately Ipa = +1.33 mA, a relatively narrow peak width (= 0.085 V), and an integrated charge of Q = 2.16 × 10^{-6} C, as shown in Table 2. When the glucose concentration increased to 5 mM, the anodic peak shifted slightly toward a more positive potential (E_{pa} = −0.010 V). The peak current remained of comparable magnitude (I_{pa} = +1.163 mA), but the peak became significantly broader (0.160 V). At higher concentrations, the transferred charge also sharply increased, suggesting a higher level of charge transfer related to oxidation.

Furthermore, at 5 mM, a secondary cathodic peak appeared (E_{pc} = 0.330 V, I_{pc} = –5.73 mA, Q = – 1.45 × 10^{-6} C), as presented in Table 4. It fits with the idea that electrochemical reduction is partially taking place on oxidized surface species and/or electroactive intermediates generated during glucose oxidation.

In general, the anodic oxidation process remains dominant, indicating a quasi-irreversible electrochemical system with measurable reverse reactions. The concentration-dependent variations—including enhanced charge transfer, increased peak broadening, slight shifts in peak potential, and the appearance of a cathodic peak suggest that the interaction between glucose and the α-Al_2O_3 electrode surface is primarily surface-controlled. At higher glucose concentrations, the electrode surface approaches saturation of active sites, at high anodic potentials, the accumulation of intermediate reactions causes a behaviour that is similar to a stop.

The result of a rise in peak height due to contributions from surface and kinetic processes, rather than purely diffusion-driven processes, results in a relatively small in-

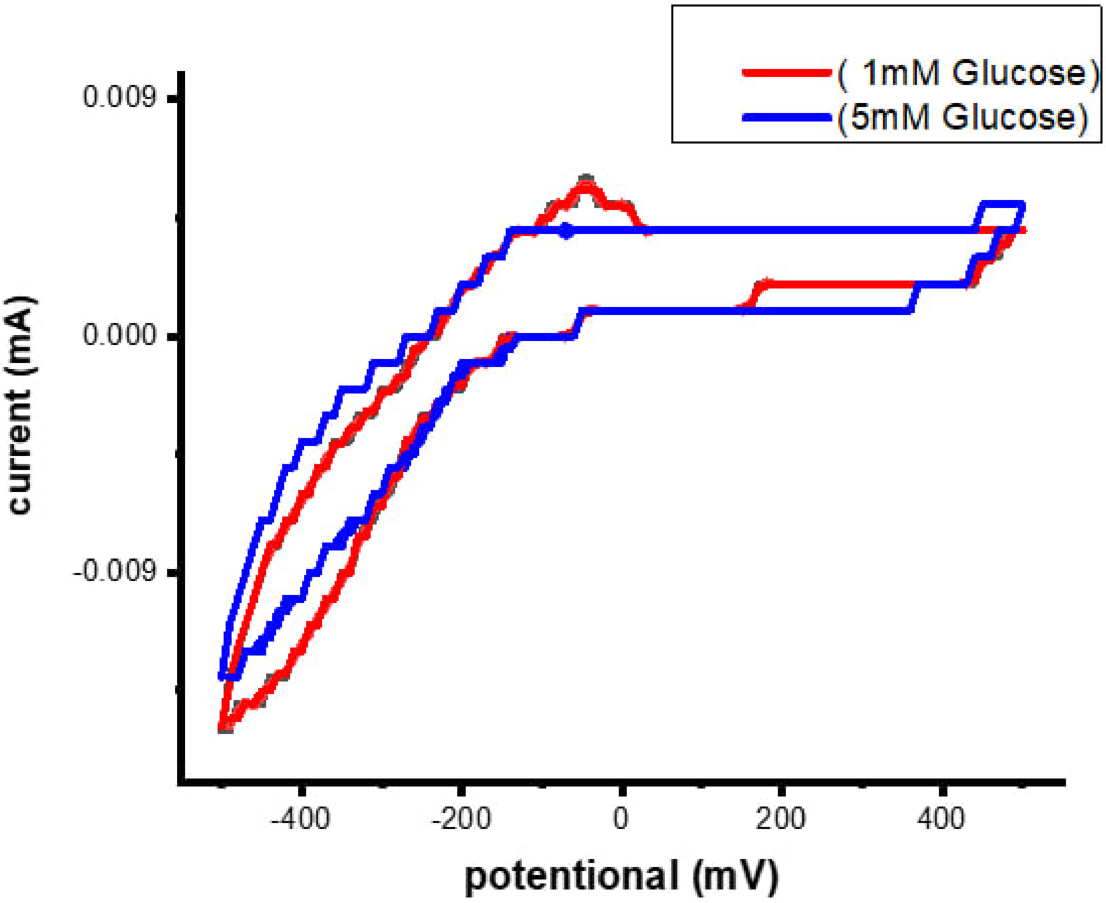

Fig. 7. Cyclic voltammetry (CV) measurements of α-AL_2O_3 NPs (1 mM, 5 mM glucose).

Table 4. Effect of concentration of glucose interaction with the α-Al_2O_3 NPs surface (charge transfer, broader peak(current), potential shift (width of peak)).

Index (No. peak)	Position of peak (V)	Height of peak (peak current) (A)	Width of peak (V)	Area peak (V*A)	Charge transfer (C)
1 (Anodic peak)	–0.05	1.34×10^{-6}	0.085	1.08×10^{-7}	2.16×10^{-6}
1 (Anodic peak)	0.01	1.32×10^{-6}	0.16	3.53×10^{-7}	7.05×10^{-6}
2 (Cathodic peak)	0.33	-5.73×10^{-7}	0.095	-7.24×10^{-8}	-1.45×10^{-6}

crease in peak current, which influences the overall response, which becomes increasingly dominant. When glucose levels are highest, various surface locations gradually become active. Therefore, kinetic constraints play an important role such as, charge-transfer resistance, surface rearrangement, and intermediate(formation) that require a slightly higher impulse for oxidation as the surface becomes more populated is further supported by the positive shift in peak potential and peak broadening at 5 mM.

The limit of detection (LOD) can be calculated from CV measurements using the following formula: Calculate the slope (S) of the calibration relation by multiplying the current peak values ($\Delta I = 0.02 \times 10^{-6}$ A) with the concentration difference($\Delta C = 4$ mM). Therefore, the slope is 5×10^{-9} A/mM and to estimate the standard deviation (SD) of the blank signal of the stable voltammogram behavior, the background current fluctuation can be reasonably estimated as: $SD = 1 \times 10^{-8}$ A also, calculate the limit of detection (LOD).

The LOD is calculated using the Eqn. 3 [37] as follow:

$$LOD = 3 \times SD/S \quad (3)$$

It is found the value of LOD to be approximately 6×10^{-3} mol/L (Mm), This value of LOD suggests that the electrode modified with α-Al_2O_3 NPs has a measurable electrochemical response to glucose, showing that it could be used in a sensing device.

4. Discussions

The XRD analysis Fig. 2 confirms that the synthesized nanoparticles possess a pure crystalline α-Al_2O_3 phase (hexagonal structure) after calcination at 900 °C, this means the synthesis conditions were optimal: high enough to stabilize the α-phase and improve crystallinity, yet controlled enough to prevent excessive grain growth and sintering. Although α-Al_2O_3 is an insulating material, the good electrochemical response observed in CV does not come from bulk electrical conductivity, instead of, it arises from surface-controlled reactions. The small crystallite size provides a large surface area and more active adsorption sites for glucose molecules, while the high crystallinity ensures a stable and reproducible electrode surface.

As a result of this balance between thermal stability and nanoscale dimensions, CV results suggest a good electrochemical performance. Moreover, the phytochemicals employed in the green synthesis improved nucleation and phase stabilization, enabling the formation of α-Al_2O_3 at a comparatively lower temperature than traditional approaches. The phase's purity and low level of impurities enhance successful electron transport at the electrode–electrolyte contact. The structural features identified by XRD (phase purity, high crystallinity, and nanoscale dimensions) directly account for the improved electrochemical performance demonstrated in the CV experiments, proving the material's applicability for glucose sensing applications.

As a result of TEM analysis Fig. 3, NPs exhibit ideal spherical morphology and a controlled size range of 12–50 nm, which is essential for improving their electrochemical properties. Through capping plant extracts (J1 and J2), particle size is significantly reduced, thereby increasing the surface-to-volume ratio and the number of electroactive sites that can be redox-cycled. Therefore, the Cyclic Voltammetry (CV) results indicate a well-defined peak current, attributable to efficient electron-transfer kinetics at the electrode interface. Additionally, the uniformity and protective layer observed in TEM images contribute to the electrode's stability and durability for a long time.

The particle size distribution of sample J1, as shown in Fig. 4, indicates that the majority of α-Al_2O_3 NPs are concentrated in the 10–15 nm range, with an average size of approximately 12 nm. The histogram demonstrates a roughly symmetric distribution, and the overlaid Gaussian curve confirms that the data follows a normal distribution pattern. This suggests that the biosynthesis method effectively controlled nanoparticle growth, minimising both excessive aggregation and the formation of extremely small or large outliers. The observed particle size range aligns well with XRD-derived crystallite sizes, supporting the high crystallinity and uniformity of the synthesized nanoparticles. Overall, these results indicate that the plant extract-mediated green synthesis method produces α-Al_2O_3 NPs with well-defined nanoscale dimensions and narrow size distribution, which are essential for consistent optical and electrochemical properties. This indicates that the plant extract effectively caps the nanoparticles and prevents agglomeration by controlling their growth.

Fig. 3 shows TEM analysis of actual nanoparticles (sample J2) and their particle size distribution. It appears that the histogram indicates that the majority of nanoparticles belong to the 20–80 nm range, with the highest frequency observed between 40–60 nm, which corresponds to the most likely particle size. According to the red fitted curve, the size distribution is relatively uniform and has a moderate degree of dispersion. A particle size under 100 nm proved that the green synthesis minimizes agglomeration by controlling particle growth.

As results that, the uniform nanoscale distribution supports the XRD and SEM findings and indicates a large surface area and active surface sites, which makes it suitable for electrochemical applications.

The FE-SEM analysis Fig. 4 revealed that the synthesized α-Al_2 O_3 NPs possessed a spherical morphology with a relatively uniform distribution and particle sizes ranging from approximately 20 to 40 nm, with average sizes of 26 nm for sample J1 and 27.9 nm for sample J2.

The images also confirmed that the nanoparticles were homogeneous, well-dispersed, and free from visible cracks or structural defects. These morphological characteristics play an important role in determining the electrochemical behaviour of the material.

The nanoscale particle size significantly increases the specific surface area, providing a larger number of active sites for electrochemical reactions. In addition, the spherical morphology and uniform distribution of the nanoparticles facilitate effective electron transfer between the electrode surface and the electrolyte. This enhanced electron transport can improve the electrochemical response observed in cyclic voltammetry measurements.

In addition, the lack of cracks and the uniform structure make the electrode material more stable and durable even after many electrochemical cycles. The FE-SEM pictures show that the synthesized α-Al_2O_{30} NPs have good structural properties that make them ideal for electrochemical applications. They may also work better in cyclic voltammetry studies.

Histogram analysis of J1 Sample, Fig. 4 represents the particle size distribution of the α-Al_2O_3 NPs synthesised using *Cinnamomum verum* extract (J1), along with a Gaussian fitting curve. The results indicate that the nanoparticles exhibit a relatively narrow size distribution, confirming a good level of uniformity in particle formation. The particle sizes are mainly distributed in the range of approximately 20 to 60 nm, with the average particle size centered around ~40 nm, as indicated by the peak of the Gaussian curve. The smooth Gaussian fitting suggests that the particles are well-dispersed and homogeneous, which is an important characteristic for improving the physical and electrochemical properties of the material. The absence of multiple peaks also indicates that there is no significant agglomeration or secondary particle population. Overall, the SEM size distribution analysis of J1 demonstrates that the green synthesis method using *Cinnamomum verum* extract is effective in producing uniform, nanoscale Al_2O_3 particles with controlled size distribution, which is desirable for advanced applications.

The particle size distribution of sample J2, as shown in Fig. 4, indicates that most α-Al_2O_3 particles are concentrated around 40 nm, with a broader size range extending from approximately 20 nm to 100 nm. The histogram demonstrates a right-shaped distribution, suggesting that tiny particles are predominant, whereas larger aggregations are also observed. In comparison to sample J1, the larger average particle size and broader distribution indicates a tendency for particle aggregation in this sample. This variation in particle size may influence the optical and electrochemical properties of the nanoparticles. The results highlight the effect of the plant extract on particle growth and aggregation, demonstrating that J2 sample produces larger and less uniform particles relative to sample of J1. The uniform morphology indicates regulated growth kinetics suggested due to the bioactive chemicals in the extract.

Performance of the synthesized α-Al_2O_3 NPs is comprehensively justified by the combined structural and morphological analyses of XRD, TEM, and SEM. The XRD confirms the formation of a pure, highly crystalline phase at 900 °C, which guarantees long-term structural stability under potential cycling. Concurrently, the TEM results confirm that the particle size was effectively restricted to the nanoscale (12–50 nm) by the plant-mediated synthesis, while the SEM images demonstrate a porous, interconnected architecture. This synergistic combination of high crystallinity, small crystallite size, and porous morphology optimizes the accessible surface area and enables rapid electron-transfer kinetics at the electrode-electrolyte interface. As a result, these structural characteristics give the synthesized nanoparticles an optimal choice for energy storage and high-sensitivity electrochemical sensing applications, superseding conventional bulk Al_2O_3 materials.

The optical properties obtained from DRS analysis in (Fig. 5 A,B) provide important insight into the electronic structure of the synthesized α-Al_2O_3 NPs, which directly influences their electrochemical behavior in cyclic voltammetry (CV) measurements. The calculated optical band gap values of 4.2 eV for J1 and 4.5 eV for J2 indicate that the nanoparticles possess a wide band gap, which is characteristic of aluminium oxide materials. Wide band gap materials typically exhibit high chemical stability and strong insulating properties, which contribute to the stability of the electrode surface during electrochemical measurements.

Although bulk α-Al_2O_3 is an electrical insulator, at nanoscale α-Al_2O_3 NPs can enhance electrochemical performance due to their high surface area and surface defects and hydroxyl groups. These features provide active sites for the adsorption of electroactive species, such as glucose molecules, on the electrode surface. As a result, electron transfer processes can occur through surface-mediated reactions, which are detectable in cyclic voltammetry experiments.

Furthermore, the slightly higher band gap observed for sample J1 (4.4 eV) compared to J2 (4.5 eV) may indicate differences in particle size, crystallinity, or surface states, which can influence the electrochemical response. These differences may contribute to variations in peak current intensity, peak position, and charge transfer behaviour observed in the CV curves. The DRS results confirm the wide band gap and optical stability of the synthesised α-Al_2O_3 NPs, while the CV measurements demonstrate their capability to participate in surface-controlled electrochemical processes, show useful they could be for electrochemical sensing applications, as in Table 5 (Ref. [18,19,20]).

The Tauc plot of α-Al_2O_3 NPs shows in (Fig. 5C,D), the appearance of two band gaps is due to defect and surface energy levels inside the forbidden gap, the first (smaller) band gap results from defect-assisted transitions, whereas the second (larger) band gap represents intrinsic valence-to-conduction band transitions, this indicates a defect-rich nanostructure that enhances charge transfer.

Microstructural investigation (SEM/TEM) generally demonstrates almost spherical or slightly irregular particles exhibiting an acceptable degree of aggregation due to increasing surface energy. The existence of lattice strain and dislocations in the crystal structure, often derived from Williamson–Hall analysis, indicates internal defects formed during rapid nucleation and growth under green synthesis conditions. These defects can improve surface activity and are beneficial for electrochemical and sensing applications. Optical investigations employing Tauc's relation usually show a broad band gap that coincides with α-Al_2O_3, meaning confirming its insulating characteristics while permitting surface charge interactions. This feature is beneficial for electrochemical sensing, because surface adsorption, rather than bulk conductivity, dictates sensing process. The green synthesis approach yields highly crystalline, nano-sized, defect-rich α-Al_2O_3 with improved surface characteristics, making it appropriate for applications like adsorption, catalysis, and electrochemical sensing (e.g., glucose detection).

4.1 FTIR Analysis of α-Al_2O_3 NPs (J1 and J2)

The FTIR spectra in Fig. 6 of the synthesized α-Al_2O_3 NPs demonstrate clear evidence of their crystalline structure, surface functional groups, and high purity. A broad absorption band at 3451 cm^{-1} (J1) and 3439 cm^{-1} (J2) corresponds to O–H stretching vibrations, indicating the presence of adsorbed water molecules or hydroxyl groups on the nanoparticle surface. Strong peaks at 457–458 cm^{-1}, 502–503 cm^{-1}, and 635–636 cm^{-1} are attributed to the Al–O stretching modes in the octahedral structure, confirming the formation of the α-phase of Al_2O_3. Additional peaks

Table 5. Comparative analysis of the current work on Al_2O_3 NPs with previous studies.

Study	Plant extract	Phase of Al_2O_3	Calcination Temp.	Particle size (nm)	Band gap (eV)	Application
Ref. [20]	Aloe vera	Amorphous	800 °C	60–100	3.8	Catalysis
Ref. [18]	Phoenix dactylifera	γ-Al_2O_3	300 °C	4–8	2.20–2.74	optical and energy storage devices
Ref. [19]	Mentha pulegium	Al_2O_3 phases	1000 °C	35	4.7	General study
This work (J1)	*Cinnamomum verum*	Pure α-Al_2O_3	900 °C	26.3	4.4	Electrochemical/Biosensing
This work (J2)	*Laurus nobilis*	Pure α-Al_2O_3	900 °C	27.9	4.5	Electrochemical/Biosensing

at 818–820 cm^{-1} correspond to Al–O stretching in tetrahedral sites, reflecting the distribution of Al and H cations within the oxide lattice. Peaks around 1000–1010 cm^{-1} indicate Al–O–H symmetric bending, showing the presence of surface hydroxyl groups, which may enhance nanoparticle stability and interaction with other molecules. Moreover, absorption bands at 1461 cm^{-1} (J1) and 1385 cm^{-1} (J2) suggest the adsorption of neutral oxygen species (O_2) on the nanoparticle surface, which is consistent with literature reports for α-Al_2O_3 NPs [19]. The absence of significant peaks corresponding to organic compounds indicates that organic impurities from plant extracts were effectively removed during high-temperature calcination, resulting in highly pure nanoparticles.

FTIR analysis suggests that the synthesized α-Al_2O_3 NPs are crystalline, structurally stable, and possess surface hydroxyl groups and adsorbed oxygen species, making them suitable for applications in electrochemical sensing, catalysis, and other surface-dependent processes.

FTIR and its relationship with Cyclic Voltammetry. The FTIR analysis of the α-Al_2O_3 NPs (J1 and J2) reveals several key surface features that directly influence their electrochemical performance. Broad bands around 3451 cm^{-1} (J1) and 3439 cm^{-1} (J2) correspond to O–H stretching vibrations, indicating the presence of hydroxyl groups or adsorbed water on the nanoparticle surfaces. These hydroxyl groups can facilitate electron transfer by providing active sites for the adsorption of electroactive molecules, such as glucose, during cyclic voltammetry. The strong peaks at 457–458 cm^{-1}, 502–503 cm^{-1}, and 635–636 cm^{-1} correspond to Al–O stretching in octahedral sites, while peaks at 818–820 cm^{-1} represent Al–O tetrahedral environments. These structural features confirm the formation of crystalline α-Al_2O_3, which provides a stable and conductive surface that enhances the reproducibility and stability of redox reactions observed in CV. Surface hydroxyls (Al–O–H at 1000–1010 cm^{-1}) and adsorbed neutral oxygen species (1461 cm^{-1} for J1, 1385 cm^{-1} for J2) create active electrochemical sites, increasing sensitivity in glucose oxidation. In CV measurements, these features manifest as well-defined anodic and cathodic peaks, where the electron transfer processes are surface-controlled. The presence of these functional groups explain why higher glucose concentrations result in peak broadening, increased current, and slight potential shifts, as more surface sites participate in the oxidation process.

FTIR confirms the presence of crystalline α-Al_2O_3 NPs with hydroxyl and oxygen species on the surface, this correlates directly with the enhanced electrochemical activity and sensitivity observed in cyclic voltammetry experiments.

The observed electrochemical behavior (cyclic volumetric) depicted in Fig. 7 this behaviour can be attributed to the role of the α-Al_2O_3 NPs coating layer, which acts as an electrochemical barrier that restricts direct charge transfer and improves the interfacial stability between the electrode and the electrolyte. As a result of this barrier effect, electron transfer processes at the electrode surface become more controlled and stable. The cyclic voltammetry response of the α-Al_2O_3 electrode changes greatly when the glucose concentration changes from 1 mM to 5 mM.

At 1 mM, a well-defined anodic oxidation peak appears at $E_{pa} = -0.050$ mV with a relatively narrow peak width and moderate charge transfer. This indicates the initial oxidation of glucose molecules adsorbed on the electrode surface.

When the glucose concentration increases to 5 mM, a slight shift of the anodic peak toward a more positive potential is observed. This shift suggests that a higher driving force is required for the oxidation process due to the increased surface coverage of glucose molecules and reaction intermediates. Additionally, the peak broadening indicates the formation and accumulation of intermediate species on the electrode surface during the oxidation reaction.

The increase in the transferred charge (Q) at higher glucose concentration reflects a greater number of electrochemical oxidation events occurring at the electrode interface. The appearance of a secondary cathodic peak at higher concentration suggests the partial electrochemical reduction of oxidized surface species or intermediates generated during glucose oxidation. The fact that the anodic oxidation signal is stronger than the others indicates that the process is almost irreversible, with only a few backward reactions possible. Also, these results suggested that the glucose oxidation process on the Al_2O_3 electrode is primarily surface-controlled, where the interaction between glucose molecules and the electrode surface plays a crucial role. At higher concentrations, active sites on the electrode surface near saturation, and the accumulation of intermediates leads to the observed plateau-like behaviour at higher anodic potentials.

Bulk α-Al_2O_3 is an electrical insulator because it has a big band gap (about 8.8 eV) and no free charge carriers. However, at the nanoscale, this behavior changes a lot. When α-Al_2O_3 is shrunk down to the size of a nanoparticle, many of the atoms are on the surface instead of in the main lattice. There are unsaturated bonds, structural flaws, and oxygen gaps in these surface atoms, which create localized energy states within the band gap. The presence of surface hydroxyl (–OH) groups derived from aqueous plant extracts further enhances the chemical activity of the nanoparticle surface. These surface of defects and functional groups contributes to the adsorption of glucose molecules and allows interfacial charge transfer processes.

The electrochemical response in α-Al_2O_3 NPs a rises not from bulk electrical conduction, but from surface-controlled charge transfer aided by defect states and adsorbed species at the nanoparticle–electrolyte interface.

4.2 Surface Adsorption Mechanism

The electrochemical behavior observed in the CV measurements suggests that the interaction between glucose molecules and the α-Al_2O_3 NPs-modified electrode is predominantly governed by a surface adsorption mechanism rather than a purely diffusion-controlled redox process. The presence of intrinsic surface peaks in the blank voltammogram indicates active surface states associated with the α-Al_2O_3 NPs. Upon the addition of glucose, noticeable peak broadening, potential shifts, and increased charge transfer were observed in the same potential regions. These changes indicate that glucose molecules are adsorbed onto the active surface sites of α-Al_2O_3, leading to modulation of the interfacial charge distribution. As the glucose concentration increases, more surface sites become occupied, resulting in enhanced surface-controlled electrochemical response and gradual saturation of active adsorption sites. This adsorption-driven mechanism explains the quasi-irreversible behavior, peak broadening, and concentration-dependent charge variation observed in the CV curves. Therefore, the electrochemical response of the α-Al_2O_3 electrode can be attributed to adsorption-mediated surface interactions between glucose molecules and the nanoparticle surface Bottom of Form.

4.3 limitations

Despite the promising outcomes obtained in the present study, several limitations remain that may restrict the practical applicability of the synthesized α-Al_2O_3 nanoparticles. First, the electrochemical glucose sensing performance demonstrated only moderate sensitivity, as evidenced by the estimated limit of detection of 6 mM. This value is considerably higher than those reported for many advanced nanostructured glucose sensors, thereby limiting the effectiveness of the material for low-concentration glucose detection.

Furthermore, the electrochemical characterization was primarily based on cyclic voltammetry measurements, while other critical sensing parameters, including selectivity, reproducibility, long-term stability, response time, and interference effects from competing biomolecules, were not comprehensively investigated. Consequently, the reliability of the sensor under practical operating conditions remains uncertain.

Another limitation is the absence of validation using real biological samples such as blood, serum, or saliva. The sensing behavior was evaluated under controlled laboratory conditions only, which may not accurately reflect the complexity of real physiological environments. Therefore, additional studies are necessary to confirm the feasibility of these nanoparticles for biomedical and clinical applications.

In addition, the synthesized samples (J1 and J2) exhibited larger crystallite sizes compared with pure Al_2O_3 nanoparticles. The increase in particle size may reduce the effective surface area available for electrochemical interactions, potentially diminishing catalytic activity and sensing efficiency. Although scanning electron microscopy revealed relatively uniform particle morphology, possible nanoparticle agglomeration during practical application cannot be excluded and may adversely affect performance stability.

Moreover, the study lacked a comprehensive comparison with commercially available glucose sensors or previously reported metal oxide nanomaterials. Such comparisons are essential for accurately evaluating the competitiveness and practical advantages of the synthesized α-Al_2O_3 nanoparticles. Finally, issues related to large-scale synthesis, batch-to-batch reproducibility, and long-term operational durability were not addressed, despite the proposed sustainability and cost-effectiveness of the green synthesis approach.

Overall, while the study successfully demonstrated the green synthesis and promising electrochemical properties of α-Al_2O_3 nanoparticles, further optimization and extensive practical validation are required before their implementation in real-world glucose sensing applications.

5. Conclusions

α-Al_2O_3 nanoparticles were produced biosynthesis using extracts from *Cinnamomum verum* and *Laurus nobilis*. The nanoparticles were uniformly distributed and ranged from 16–33 nm in size. They had a high UV absorption rate and a single-phase structure. FTIR examination indicates that the bio reduction of Al^{3+} ions and stability of nanoparticles may have occurred because of interactions between the bio-functional groups in *Cinnamomum verum* and *Laurus nobilis* extract and aluminum. The plant products worked as natural caps, keeping the particles from sticking together and making them more biocompatible. CV studies showed that the surface of these eco-friendly α-Al_2O_3 nanoparticles had an electrochemical response to glucose that was almost irreversible and measurable charge transfer. This showed that the nanoparticles could be used for sensing, medicinal, and photocatalytic purposes.

Availability of Data and Materials

The datasets used and/or analyzed during the current study are available from the corresponding author on reasonable request.

Author Contributions

The research study was designed by HAATAO and LKA. NJJ and HAATAO carried out experiments. LKA and NJJ assisted with the experiments. HAATAO analysed the data. All authors contributed to editorial changes in the manuscript. The final manuscript was read and approved by all authors, who all had a sufficient amount of involvement in the work and agreed to be responsible for all aspects thereof.

Ethics Approval and Consent to Participate

Cinnamomum verum (J1) and Laurel leaves (J2). Plants were used in this study from the market, Wasit, Iraq.

Acknowledgment

The authors would like to express their sincere appreciation to all those who provided support and assistance during the completion of this research work. Their valuable contributions during the experimental study and preparation of this manuscript are gratefully acknowledged.

Funding

This research received no external funding.

Conflicts of Interest

The authors declare no conflicts of interest.

References

[1] Mohammed AA, Khodair ZT, Khadom AA. Preparation and investigation of the structural properties of α-Al2O3 nanoparticles using the sol-gel method. Chemical Data Collections. 2020; 29: 100531. https://doi.org/10.1016/j.cdc.2020.100531

[2] Falcón-Castrejón RA, Román-Zubillaga JL, Guardián-Tapia R, Falcón-Franco L, Rosales-Cadena I. Synthesis and Characterization of Aluminum Alloys with Metal Oxides (CuO2) Additions as Reinforcement. Materials Sciences and Applications. 2023; 14: 416–425. https://doi.org/10.4236/msa.2023.148027

[3] Pehlivan M, Simsek S, Ozbek S, Ozbek B. An extensive study on the synthesis of iron based magnetic aluminium oxide nanocomposites by solution combustion method. Journal of Materials Research and Technology. 2019; 8: 1746–1760. https://doi.org/10.1016/j.jmrt.2018.12.005

[4] Zhang D, Nastac L. Numerical modeling of the dispersion of ceramic nanoparticles during ultrasonic processing of aluminum-based nanocomposites. Journal of Materials Research and Technology. 2014; 3: 296–302. https://doi.org/10.1016/j.jmrt.2014.09.001

[5] Karaman C, Karaman O, Atar N, Yola ML. A molecularly imprinted electrochemical biosensor based on hierarchical Ti2Nb10O29 (TNO) for glucose detection. Mikrochimica Acta. 2021; 189: 24. https://doi.org/10.1007/s00604-021-05128-x

[6] Mohamad Nor N, Ridhuan NS, Abdul Razak K. Progress of Enzymatic and Non-Enzymatic Electrochemical Glucose Biosensor Based on Nanomaterial-Modified Electrode. Biosensors. 2022; 12: 1136. https://doi.org/10.3390/bios12121136

[7] Jena BK, Raj CR. Enzyme-free amperometric sensing of glucose by using gold nanoparticles. Chemistry (Weinheim an Der Bergstrasse, Germany). 2006; 12: 2702–2708. https://doi.org/10.1002/chem.200501051

[8] Han Y, Guo Y, Gu J. Thermally conductive fillers. Thermally Conductive Polymer Composites. 2023; 111–147. https://doi.org/10.1016/b978-0-323-95231-6.00002-7

[9] Karakassides MA, Gournis D, Bourlinos AB, Trikalitis PN, Bakas T. Magnetic Fe2O3–Al2O3 composites prepared by a modified wet impregnation method. Journal of Materials Chemistry. 2003; 13: 871–876. https://doi.org/10.1039/b211330a

[10] Ali AO, El Naggar AM, Morshedy AS, Aboutaleb WA, Metwally NH. Synthesis and characterization of iron-alumina composites as novel efficient photocatalysts for removal of DBT. Chemosphere. 2022; 307: 136011. https://doi.org/10.1016/j.chemosphere.2022.136011

[11] Nasrollahzadeh M, Issaabadi Z, Sajadi SM. Green synthesis of Cu/Al2O3 nanoparticles as efficient and recyclable catalyst for reduction of 2,4-dinitrophenylhydrazine, Methylene blue and Congo red. Composites Part B: Engineering. 2019; 166: 112–119. https://doi.org/10.1016/j.compositesb.2018.11.113

[12] Wu M, Ni L, Lu H, Xu H, Zou S, Zou X. Terpenoids and Their Biological Activities from Cinnamomum: A Review. Journal of Chemistry. 2020; 2020: 1–14. https://doi.org/10.1155/2020/5097542

[13] Phu HH, Pham Van K, Tran TH, Pham DTN. Extraction, Chemical Compositions and Biological Activities of Essential Oils of Cinnamomum verum Cultivated in Vietnam. Processes. 2022; 10: 1713. https://doi.org/10.3390/pr10091713

[14] Awada F, Hamade K, Kassir M, Hammoud Z, Mesnard F, Rammal H, et al. Laurus nobilis Leaves and Fruits: A Review of Metabolite Composition and Interest in Human Health. Applied Sciences. 2023; 13: 4606. https://doi.org/10.3390/app13074606

[15] Çam ST, Aydaş C, Engin B, Yüce ÜR, Aydın T, Polat M. ESR and TL studies of irradiated Anatolian laurel leaf (Laurus nobilis L.). Radiation Effects and Defects in Solids. 2012; 167: 410–420. https://doi.org/10.1080/10420150.2012.666243

[16] Caputo L, Nazzaro F, Souza LF, Aliberti L, De Martino L, Fratianni F, et al. Laurus nobilis: Composition of Essential Oil and Its Biological Activities. Molecules (Basel, Switzerland). 2017; 22: 930. https://doi.org/10.3390/molecules22060930

[17] Al-Ogaili HAT, Jubier NJ, Thamer AA. Comparative study of Raman modes active, emission bands and thermal features of GSA-Al2O3 NP's. Digest Journal of Nanomaterials and Biostructures. 2025; 20: 365–372. https://doi.org/10.15251/djnb.2025.201.365

[18] Saleh AK, Shaban AS, Diab MA, Debarnot D, Elzaref AS. Green synthesis and characterization of aluminum oxide nanoparticles using Phoenix dactylifera seed extract along with antimicrobial activity, phytotoxicity, and cytological effects on Vicia faba seeds. Biomass Conversion and Biorefinery. 2024; 14: 31859–31875. https://doi.org/10.1007/s13399-023-04800-x

[19] Babiker MEM. Eco-Environmentally Friendly Green Synthesis and Characterization of Aluminum Oxide Nanoparticles Using Leaf Extract of Mentha Pulegium. International Journal of Chemical and Biochemical Sciences. 2024; 25. https://doi.org/10.62877/114-ijcbs-24-25-19-114

[20] Al-Sumaidaie GJK, AL-Doury MMI. Removal of Phosphate Ions from Aqueous Solution by Al2O3 Nanoparticles Loaded on Activated Carbon Synthesized from Aloe Vera Gum. Tikrit Journal of Engineering Sciences. 2025; 32: 1–17. https://doi.org/10.25130/tjes.32.3.2

[21] Nemade K, Tekade P, Dudhe P. Strengthening of photovoltaic and supercapacitive properties of graphene oxide-polyaniline composite by dispersion of α-Al2O3 nanoparticles. Chemical Physics Letters. 2018; 706: 647–651. https://doi.org/10.1016/j.cplett.2018.07.018

[22] Liu J, Guo Q, Yu M, Li S. Effect of TiO2 nanostructures on specific capacitance of Al2O3–TiO2 composite film on etched aluminum foil formed by the sol–gel and anodizing. Ceramics International. 2014; 40: 3687–3692. https://doi.org/10.1016/j.ceramint.2013.09.056

[23] Kusuma K, Manju M, Ravikumar C, Nagaswarupa H, Amulya MS, Anilkumar M, et al. Photocatalytic and electrochemical sensor for direct detection of paracetamol comprising γ-aluminium oxide nanoparticles synthesized via sonochemical route. Sensors International. 2020; 1: 100039. https://doi.org/10.1016/j.sintl.2020.100039

[24] Bokhary KA, Maqsood F, Amina M, Aldarwesh A, Mofty HK, Al-Yousef HM. Grapefruit Extract-Mediated Fabrication of Photosensitive Aluminum Oxide Nanoparticle and Their Antioxidant and Anti-Inflammatory Potential. Nanomaterials (Basel, Switzerland). 2022; 12: 1885. https://doi.org/10.3390/nano12111885

[25] Tran GT, Nguyen NTH, Nguyen NTT, Nguyen TTT, Nguyen DTC, Tran TV. Plant extract-mediated synthesis of aluminum oxide nanoparticles for water treatment and biomedical applications: a review. Environmental Chemistry Letters. 2023; 21: 2417–2439. https://doi.org/10.1007/s10311-023-01607-0

[26] Shafqat S, Munir H, Najeeb J, Naseem K, Irfan M. Fabrication of Multifaceted Alpha-Alumina Nanoparticles: Exploring Bioactive and Photocatalytic Properties. BioNanoScience. 2025; 15. https://doi.org/10.1007/s12668-025-01839-0

[27] Kamil F, Hubiter KA, Abed TK, Al-Amiery AA. Synthesis of aluminum and titanium oxides nanoparticles via sol-gel method: optimization for the minimum size. Journal of Nanoscience and Technology. 2016; 2: 37–39.

[28] Behera PS, Sarkar R, Bhattacharyya S. Nano Alumina: A Review of the Powder Synthesis Method. Interceram - International Ceramic Review. 2016; 65: 10–16. https://doi.org/10.1007/bf03401148

[29] Kaczmar J, Pietrzak K, Włosiński W. The production and application of metal matrix composite materials. Journal of Materials Processing Technology. 2000; 106: 58–67. https://doi.org/10.1016/s0924-0136(00)00639-7

[30] Ghotekar S. Plant extract mediated biosynthesis of Al2O3 nanoparticles-a review on plant parts involved, characterization and applications. Nanochemistry Research. 2019; 4: 163–169. https://doi.org/10.22036/ncr.2019.02.008

[31] Yamamura K, Hama M, Kobayashi Y, Yasuda Y, Morita T. Effect of hydrothermal process for inorganic alumina sol on crystal structure of alumina gel. Journal of Asian Ceramic Societies. 2016; 4: 263–268. https://doi.org/10.1016/j.jascer.2016.05.002

[32] Prashanth P, Raveendra R, Hari Krishna R, Ananda S, Bhagya N, Nagabhushana B, et al. Synthesis, characterizations, antibacterial and photoluminescence studies of solution combustion-derived α-Al2O3nanoparticles. Journal of Asian Ceramic Societies. 2015; 3: 345–351. https://doi.org/10.1016/j.jascer.2015.07.001

[33] Naayi SA, Hassan AI, Salim ET. FTIR and X-ray diffraction analysis of Al2O3 nanostructured thin film prepared at low temperature using spray pyrolysis method. International Journal of Nanoelectronics and Materials. 2018; 11: 1–6.

[34] Djebaili K, Mekhalif Z, Boumaza A, Djelloul A. XPS, FTIR, EDX, and XRD Analysis of Al2O3Scales Grown on PM2000 Alloy. Journal of Spectroscopy. 2015; 2015: 1–16. https://doi.org/10.1155/2015/868109

[35] Feng K, An J, Ren W, Lei X, Li G, Rong D, et al. The synthesis of urchin-like γ-Al2O3 hierarchical microspheres from Al foils and its rapid adsorption ability towards Congo red. Materials Research Express. 2020; 7: 035011. https://doi.org/10.1088/2053-1591/ab7a62

[36] Razak EA, Al-Ogaili HAT. Bio fabrication techniques, optical characteristics and applications of TiO2 in the environmental and medical sector. Digest Journal of Nanomaterials and Biostructures. 2025; 20: 681–690. https://doi.org/10.15251/djnb.2025.202.681

[37] Wahab R, Alam M. Highly efficient and fast electrochemical sensor based on aluminium oxide (Al2O3) nanoparticle for the detection of organosulfur compounds. Sensors and Actuators A: Physical. 2022; 347: 113967. https://doi.org/10.1016/j.sna.2022.113967